Marine and Petroleum Geology 109 (2019) 899–911

Contents lists available at ScienceDirect

Marine and Petroleum Geology

journal homepage: www.elsevier.com/locate/marpetgeo

Research paper

Physical properties of fine-grained sediments with segregated hydrate lenses

Liang Lei[a,*], J. Carlos Santamarina[b]

[a] National Energy Technology Laboratory, U.S. Department of Energy, Morgantown, WV, 26507, USA
[b] Earth Science and Engineering, KAUST, Thuwal, Saudi Arabia

ARTICLE INFO

Keywords:
Fine-grained sediments
Hydrate lenses
Cryogenic suction
Gas production
Slope stability

ABSTRACT

The physical properties of natural gas hydrate-bearing sediments are critical for the analysis of natural systems and for the design of gas production strategies. This work explores the properties of fine-grained sediments containing segregated hydrate lenses. Our analyses show that hydrate formation is grain-displacive when the product of the effective stress and the grain radius is $\sigma' R < 2\pi\Gamma_{hw} \approx$ 0.2-to-0.3 N/m, such as in shallow fine-grained sediments. The assessment of physical properties is particularly challenging in fine-grained sediments with segregated gas hydrate because (1) inherent difficulties in hydrate formation hinder laboratory studies, and (2) segregated hydrate requires large specimens and laboratory devices to avoid boundary effects and to create a representative volume for analysis. We circumvent these challenges through the use of numerical simulations. In these simulations, the properties of the hydrate-free sediment surrounding the segregated hydrate lenses take into consideration the effects of cryogenic suction and grain-displacive hydrate growth. Our results for mechanical properties and conduction show that numerical simulations must properly consider the hydrate morphology, the altered sediment properties, and the sediment-hydrate interfacial conditions (interfaces are rough, jagged and well bonded during hydrate formation, but become weak-frictional on dissociation). In fact, changes in the strength and stiffness of the hydrate-free sediment that surrounds a segregated hydrate mass can be more important on the global properties than the presence of hydrate itself. Numerical simulations highlight distinct anisotropy in mechanical properties and conduction in the presence of segregated hydrate lenses, and the tendency to shear localization when there is a weak-frictional interface. We emphasize that a relatively small fraction of fines can make sediments prone to segregated hydrate formation, therefore proper sediment classification is critical.

1. Introduction

Gas hydrate accumulations in marine sediments and the permafrost are a vast potential energy resource (Boswell, 2009; Collett, 2002). In addition, natural gas hydrate dissociation can contribute to climate change (Archer, 2007; Ruppel and Pohlman, 2008), cause ground subsidence and trigger seafloor landslides (Grozic, 2010; Hornbach et al., 2007; Kvalstad et al., 2005).

The mechanical, thermal, and hydraulic properties of gas hydrate-bearing sediments are critical to both the analysis of natural gas hydrate reservoirs and the design of gas extraction strategies. The transmission of heat and fluids control hydrate dissociation and gas migration (Makogon, 1997; Sloan and Koh, 2007). In addition, the mechanical properties of hydrate-bearing sediments can be markedly different before and after dissociation, thus, initially stable systems can become unstable during hydrate dissociation (Kwon et al., 2008; Moridis et al., 2011; Waite et al., 2009).

A number of difficulties limit the accurate characterization and direct measurement of the physical properties of hydrate-bearing sediments. Pressure cores are expensive, and mechanical sampling disturbances are inherent to all coring techniques (Dai and Santamarina, 2014; Hvorslev, 1949). In-situ measurements only assess a small area around the well-logging tool, which is disturbed by the insertion of the device itself. Laboratory hydrate formation is challenging in all sediments (Spangenberg et al., 2005; Waite and Spangenberg, 2013), particularly in fine-grained sediments (Lei and Santamarina, 2018). Furthermore, hydrate tends to form as a segregated mass in fine-grained sediments and the length-scale of natural hydrate lenses and veins exceeds the centimeter-scale of laboratory devices (Collett et al., 2008; Lee et al., 2013; Yamamoton et al., 2012; Yun et al., 2011). Studies of physical properties of hydrate-bearing fine-grained sediments are thus limited to geophysical logs, e.g. (Cook et al., 2008; Tréhu et al., 2004), some pressure core based measurements (Yun et al., 2011), and numerical simulations that explore segregated hydrate geometries but neglect the effect of hydrate formation on surrounding sediments (Ghosh et al., 2010).

Most hydrate accumulations involve fine-grained sediments (Boswell and Collett, 2011). Therefore, there is a need for an enhanced

* Corresponding author.
E-mail address: liang.lei@netl.doe.gov (L. Lei).

https://doi.org/10.1016/j.marpetgeo.2019.08.053
Received 19 February 2019; Received in revised form 24 August 2019; Accepted 30 August 2019
Available online 03 September 2019

understanding of the physical properties of hydrate-bearing fine-grained sediments. This study uses numerical simulations to estimate the conductivity, stiffness and strength of sediments with segregated hydrate lenses. In particular, we take into consideration the effects of grain-displacive hydrate formation and cryogenic suction on the properties of the surrounding hydrate-free sediments, and explore different hydrate morphologies observed in natural fine-grained sediments. The final section discusses the dominant effect of fines on the sediment response, assesses the applicability of effective media models and theoretical bounds, and summarizes lessons learned from this study into a procedure to estimate the physical properties of fine-grained hydrate-bearing sediments.

2. Segregated hydrate in fine-grained sediments

Hydrate nucleates on mineral grain surfaces or at gas-water interfaces and eventually fills pores in coarse-grained sediments (Waite et al., 2009). However, field evidence shows that hydrate displaces grains in fine-grained sediments and forms segregated lenses, veins and nodules (Dai et al., 2012).

Pore-invasive versus grain-displacive hydrate formation reflects the balance between particle-level forces. Fig. 1 shows a particle-level free body diagram of sediment particles, the hydrate mass and pore water, where the hydrate-water interface is at the verge of invading pores. The hydrate mass is non-wetting (Lei et al., 2019), feels a pressure P_h higher than the water pressure u_w, and presses against sediment grains. In addition to the grain's self-weight, three forces act on a grain of radius R: (1) the force that results from the hydrate-water pressure difference against the grain's cross-sectional area $C_\Delta = (P_h\text{-}u_w)\cdot\pi R^2$ for water-wet mineral surfaces with zero contact angle, (2) the pull from the hydrate-water interfacial tension Γ_{hw} around the grain perimeter $C_\Gamma = \Gamma_{hw}\cdot 2\pi R$, and (3) the skeletal force $N \approx \sigma'\cdot(2R)^2$ that the grain must carry for being part of the granular skeleton subjected to effective stress σ' (assumes a simple cubic packing - Santamarina, 2001). The Laplacian hydrate-water pressure difference is $(P_h\text{-}u_w) = 2\Gamma_{hw}/R_{pore}$ (Clennell et al., 1999). The pore radius R_{pore} is a function of the grain radius R; in general, the ratio $\alpha = R_{pore}/R$ also depends on particle shape, size distribution, and packing.

The hydrate mass will displace grains when $(C_\Delta + C_\Gamma) > N$. Let's consider uniform round grains so that α = 0.3-to-0.4 (Santamarina et al, 2001), and hydrate-water interfacial tension Γ_{hw} = 0.032-to-0.039 N/m (Anderson et al., 2003; Uchida et al., 1999). Then, the limiting equilibrium analysis anticipates displacive hydrate formation when

$$\sigma' R < 2\pi\Gamma_{hw} \approx 0.2 - \text{to} - 0.3\ \text{N/m} \tag{1}$$

Consequently, fine-grained sediments (small R) and/or shallow formations (low σ') are prone to the formation of segregated hydrate lenses and nodules, in agreement with field observations (Dai et al., 2012).

2.1. Hydrate morphology: observations from previous work

Fig. 2 presents a collection of X-ray projections and CT slices of fine-grained sediments recovered using pressure coring technology. Fig. 3 shows photographic images of recovered fine-grained sediments after rapid depressurization. The hydrate mass is segregated in all cases, varies from sub-millimeter to multi-centimeter thicknesses, and the length scale clearly exceeds the core diameter. Overall, the complex hydrate morphologies observed in Figs. 2 and 3 combine elemental configurations such as parallel and intersecting lenses. The hydrate-sediment interface is not smooth; in fact, the shape of the hydrate mass is quite irregular and jagged. Laboratory investigations show that hydrate can form in gas-driven fractures where it inherits the fracture morphology, including rough edges and uneven propagation fronts (Fig. 4).

2.2. Hydrate volume fraction

The degree of hydrate saturation in pore-filling coarse-grained sediments $S_h = V_h/V_v$ relates the volume of hydrate V_h to the overall volume of voids V_v. However, the ratio $F_h = V_h/V_t$ between the segregated hydrate volume V_h and the total sediment volume V_t is a more convenient and intuitive definition for particle-displacive hydrate accumulations in fine-grained sediments (Note: the value F_h applies to coarse-grained sediments as well). Clearly, both definitions are related through the global porosity $F_h/S_h = n$. Some of the images in Figs. 2 and 3 correspond to near-seafloor accumulations and exhibit very high hydrate volume fractions in excess of $F_h > 40\%$. Low effective stress and high sediment compressibility favor thicker lenses.

3. Surrounding sediment: compaction and stress changes

Displacive hydrate formation alters the state of stress and compresses the surrounding hydrate-free sediment. In this section, we use analytical solutions to examine the induced volumetric strains and stress changes on the surrounding hydrate-free sediment as a function of the hydrate volume fraction F_h and boundary conditions. We identify five end-member conditions to allow for tractable solutions and scale-analyses. Field situations will often involve more complex conditions that require case-specific analyses.

3.1. Formation from initial excess dissolved methane (closed system)

The solubility of CH_4 in water rises with increasing pressure and decreasing temperature (Henry's law approximation). The presence of hydrates favors further hydrate formation and there is a decrease in gas concentration in water after hydrate formation (Henry et al., 1999; Lu et al., 2008; Waite et al., 2009). The difference between the gas concentration before hydrate formation C^b and after hydrate formation C^a

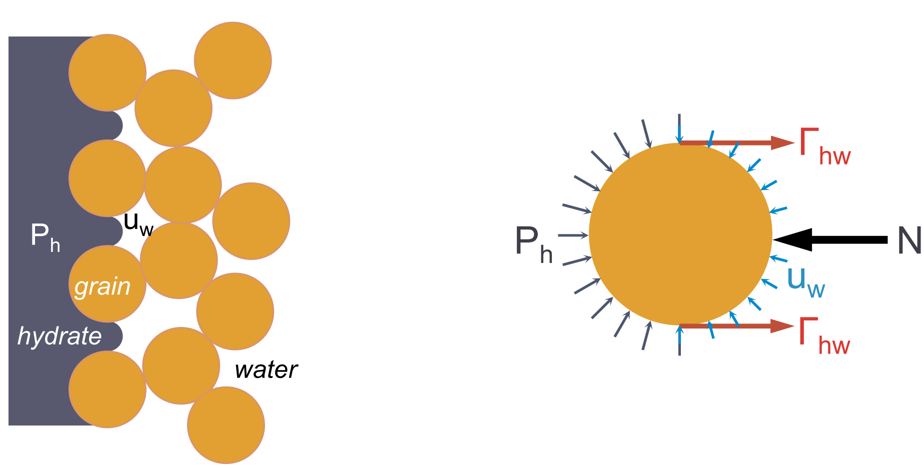

Fig. 1. Particle-scale force equilibrium at the verge of hydrate invasion. The skeletal force N is carried by the particle because it is part of a granular skeleton subjected to effective stress σ'. The capillary force involves the pressure in the non-wetting hydrate mass P_h, the water pressure u_w, and the surface tension between hydrate and water Γ_{hw}.

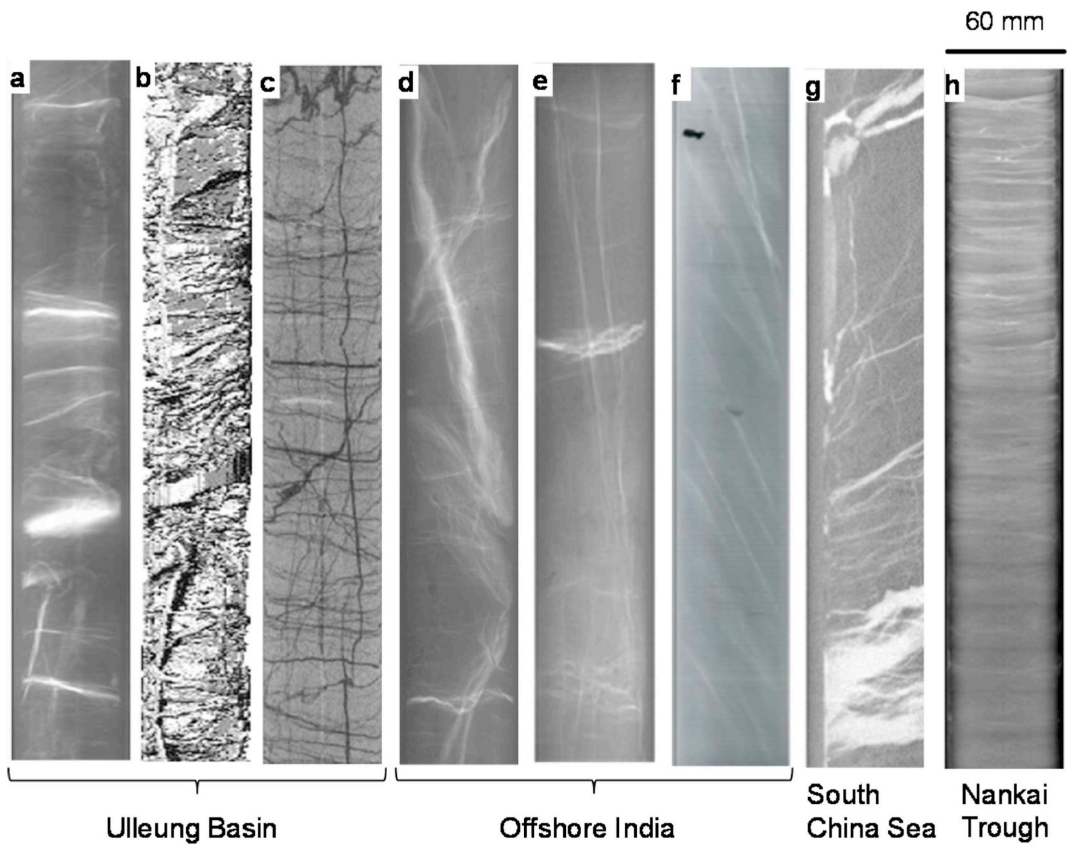

Fig. 2. Natural specimens with segregated hydrate in fine-grained sediments. (a, d, e, f, g, h) X-ray projections: bright areas correspond to the low-density hydrate mass. (b) 3D CT scan rendition of the segregated hydrate, where the sediment is made transparent. (c) Slice of a 3D CT scan – segregated hydrate lenses appear as dark lines. Sources: [a,b,c](Lee et al., 2011); [d](Collett et al., 2008); [e](Rees et al., 2011); [f](Boswell et al., 2007); [g](Zhang et al., 2014); [h](Yamamoton et al., 2012).

can be used to compute the hydrate volume fraction that can form in a sediment with an initial porosity n_0

$$F_h = \frac{V_h}{V_t} \approx \frac{C^b - C^a}{C^H} n_0 \tag{2}$$

where $C^H = 8.79\,\mathrm{mol/cm^3}$ ($CH_4 \bullet 6H_2O$) is the concentration of methane in hydrate, and superscripts b and a refer to before and after hydrate formation. The gas concentration C^b can be higher in the nano pores of high specific surface sediments than in bulk fluids (for example, 50% higher in 10 nm pores). Before hydrate formation, the concentration of CH_4 in water can reach C^b ~0.08-to-0.20 mol/kg (for PT conditions P < 25 MPa and T < 15 °C). The concentration of gas in water after hydrate formation is approximately half of the gas concentration in water in the absence of hydrate (Duan and Mao, 2006; Duan and Sun, 2003). Order of magnitude analyses for sediments at a water pressure of 20 MPa show that the volume fraction of segregated hydrate that forms from dissolved gas ranges between $F_h = 0.6\%$ for low specific surface kaolinites at 50 mbsf and 4 °C, to more than $F_h = 1.7\%$ for a montmorillonitic layer at 250 mbsf and 9 °C (Jang and Santamarina, 2016b).

Displacive hydrate compresses the sediment when formation takes place under zero-lateral strain boundary conditions. The volumetric strain in the surrounding sediment is (1D configuration):

$$\varepsilon_{vol} = \frac{\Delta L}{L} = \frac{e^b - e^a}{(1 + e^b)} = F_h \tag{3}$$

Sediment compaction under isotropic or zero-lateral strain conditions follows Terzaghi's consolidation model. The change in void ratio e^b-e^a from the initial void ratio e^b before hydrate formation under effective stress σ'^b, to void ratio e^a after hydrate formation reflects the associated change in effective stress,

$$e^b - e^a = C_c \log\left(\frac{\sigma'^a}{\sigma'^b}\right) \tag{4}$$

where σ'^a is the effective stress in the sediment after hydrate formation and C_c is the compression index of hydrate free sediments. Equations (3) and (4) combine to anticipate the change in stress in the hydrate-free sediment that surrounds the hydrate mass:

$$\log\left(\frac{\sigma'^a}{\sigma'^b}\right) = F_h \frac{(1 + e^b)}{C_c} \tag{5}$$

For example, a hydrate saturation of $F_h = 5\%$ will cause a 40% increase in stress in the fine-grained sediments from the Ulleung basin, $\sigma'^a/\sigma'^b = 1.4$ ($C_c = 1.19$, and in situ void ratio $e_o = 2.2$ - Lee et al., 2011), and a 60% increase in the Hydrate Ridge formation, $\sigma'^a/\sigma'^b = 1.6$ ($C_c = 0.568$, $e_o = 1.35$ - Tan et al., 2006).

3.2. Water-limited hydrate formation (water and mineral mass conservation)

The previous analysis assumed no external gas supply. Next, consider gas supply via gas-driven fractures. Gas invasion forms gas-filled fractures in fine-grained sediments when the capillary pressure difference between the gas and pore water exceeds the effective stress (Shin and Santamarina, 2011; Sun and Santamarina, 2019). After gas invasion, hydrate formation extracts water from the surrounding sediment and causes sediment compaction similar to cryogenic suction (Fig. 5). Equations (3) and (4) predict the ensuing changes in effective stress and void ratio.

Fig. 3. Natural specimens with segregated hydrate in fine-grained sediments, photographed immediately after recovery and fast depressurization. Sources: (a, b, e, f) image courtesy of NGHP 01; (c) Park et al., 2008; (d) Zhang et al., 2014; (g, i) courtesy of Oleg Khlvstov; (h, j, k, l) courtesy of GEOMAR.

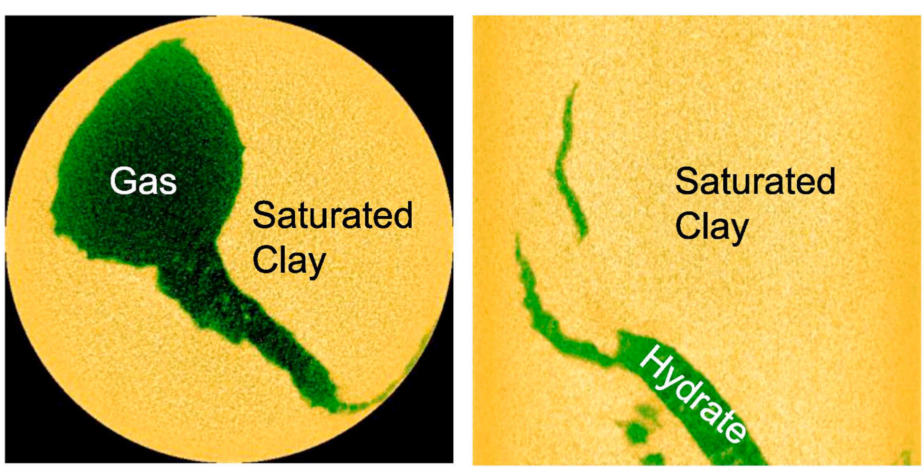

Fig. 4. Slice of a micro-CT tomogram showing segregated hydrate growth within a gas-driven fracture in a clayey sediment (Laboratory study documented in Lei and Santamarina, 2018).

3.3. Near-surface vertical lenses

The state of stress near the seafloor is typically in a "k_o-condition", hence, the vertical effective stress is the major principal stress $\sigma'_z = \sigma'_1$ and the horizontal effective stress is $\sigma'_{hor} = k_o\sigma'_z$ where $k_o \approx$ 1-sinϕ and ϕ is the sediment friction angle (Mayne and Kulhawy, 1982; Shin and Santamarina, 2009). The increase in horizontal stress due to hydrate formation depends on the lens length-to-spacing ratio L/s. For long and

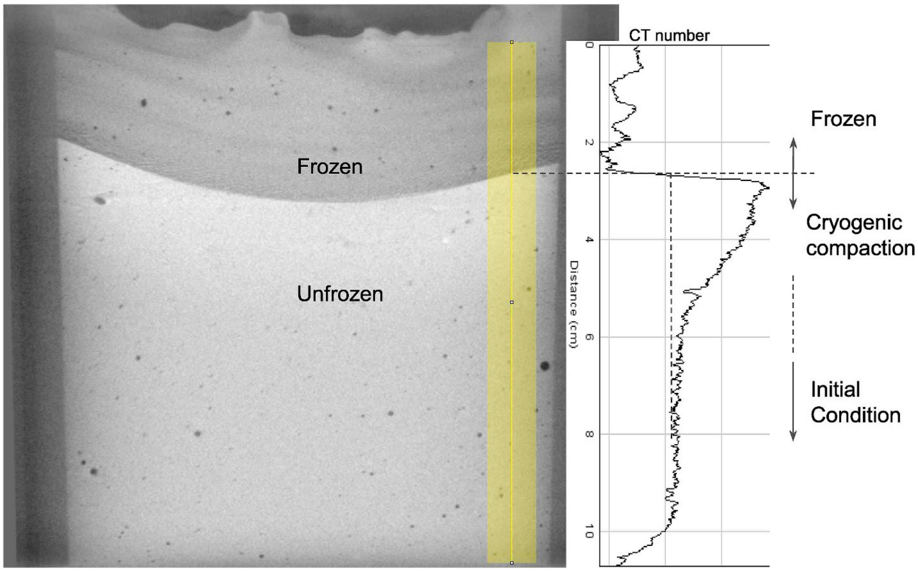

Fig. 5. Cryogenic suction during ice formation in a kaolinite paste specimen as the freezing front advances from the top. (a) Vertical slice of a micro-CT tomogram. (b) The CT number measured along the vertical line highlighted in the tomographic slice (Note: the CT number correlates with density). From top to bottom: ice dominant "frozen" zone, kaolinite compacted by cryogenic suction, and kaolinite at the initial condition (after Viggiani et al., 2015).

parallel lenses $L/s > 1$, the zero lateral strain condition applies and the stress ratio and associated void ratio changes evolve as predicted by Equations (2) and (4).

For high separation $L/s < 1$, the maximum increase in horizontal effective stress against the lens relates to the stress ratio at passive failure $k_p = (1+\sin\phi)/(1\text{-}\sin\phi)$. Therefore, the maximum anticipated increase in the horizontal effective stress against a vertical lens is

$$\left.\frac{\sigma'^{a}_{hor}}{\sigma'^{b}_{hor}}\right|^{max} = \frac{k_p}{k_o} = \frac{1+sin\phi}{(1-sin\phi)^2} \tag{6}$$

where superscripts b and a refer to before and after hydrate formation. For typical fine-grained marine sediments with $\phi = 15°\text{-to-}25°$, the horizontal effective stress after hydrate formation could be 2 to 4 times higher than before hydrate formation. As a first-order approximation, let's consider Terzaghi's consolidation model here as well $e^b\text{-}e^a = C_c\log(\sigma'^a/\sigma'^b)$, where σ'^a/σ'^b is obtained from Equation (6). Then, we can anticipate a decrease in void ratio $e^b\text{-}e^a = 0.36\text{-to-}0.72$ for the Ulleung Basin sediments, and $e^b\text{-}e^a = 0.17\text{-to-}0.34$ for Hydrate Ridge sediments (compressibility values C_c from Lee et al., 2011 and Tan et al., 2006).

3.4. Near-surface horizontal lenses

Lenses will grow along horizontal layers when stratigraphy rather than stress controls hydrate formation, such as observed at the Sea of Okhotsk (Shoji et al., 2005) and Hydrate Ridge (Bohrmann et al., 2002). The burial depth H determines the normal vertical effective stress on long and shallow horizontal lenses $L/H \gg 1$, and the vertical effective stress and void ratio may remain constant provided that fluids can migrate faster than the rate of hydrate formation.

3.5. Deep lenses

Finally, consider a short, isolated lens of thickness t_h, far from the sediment free surface ($L/H \ll 1$). The lens growth and expansion causes a stress increment normal to the lens; from the theory of elasticity (plain strain condition – Gdoutos, 2006)

$$(\sigma'^a - \sigma'^b)_{nor} = \frac{G}{1-\nu}\frac{t_h}{L} \tag{7}$$

Associated void ratio changes relate to the vertical strain increment (drained condition)

$$\varepsilon_{norm} = \frac{\Delta e}{1+e^b} = \frac{(\sigma'^a - \sigma'^b)_{nor}}{E} = \frac{G}{1-\nu}\frac{t_h}{L}\frac{1}{2G(1+\nu)} = \frac{t_h}{L}\frac{1}{2(1-\nu^2)} \tag{8}$$

where the elastic parameters of the virgin hydrate free sediments are Poisson's ratio ν and the shear modulus G. Note that the shear modulus is a function of the effective stress in sediments. Whereas previous cases assumed 1D-conditions, here we analyze a short isolated lens; in this case, Equation (8) predicts that the change in effective stress is a function of the hydrate lens geometry.

3.6. Concluding remarks on surrounding sediments

In conclusion, deformation and fluid-flow boundary conditions determine the stress and void ratio changes in the sediment that surrounds segregated hydrate masses. In all cases, void ratio and effective stress changes are proportional to the hydrate volume fraction F_h.

4. Surrounding sediment: properties after lens formation

The sediment void ratio and effective stress after hydrate formation help us estimate the physical properties of the hydrate-free sediment that surrounds hydrate lenses, including stiffness, strength and conductivities (thermal, hydraulic and electrical). Table 1 lists a selection of robust physics-based correlations between the properties of the surrounding sediment after hydrate formation and the sediment properties before hydrate formation, collected from published work. These correlations rely on information such as the effective stress and/or porosity obtained from the previous analyses. Stiffness and strength increase with effective stress. Thermal, hydraulic and electrical conductivities respond to changes in the volume fraction of water, i.e., void ratio e or porosity n.

The stiffness, strength, and thermal conductivity are higher after hydrate formation. On the other hand, the sediment hydraulic conductivity decreases during compaction. The evolution of the electrical conductivity is complex and combines: reduction in porosity, early increase in fluid electrical conductivity due to ion-exclusion, and time-dependent excess ion diffusion into the far field.

5. Numerical Simulations – Results

We used COMSOL, a commercially available multi-physics simulator, to study Laplacian fields and Abaqus for mechanical properties including stiffness and strength. In both cases, we optimized mesh resolution and confirmed numerical models against available analytical solutions. Table 2 lists the parameters used in the numerical simulations. Values before and after hydrate formation are consistent with the

Table 1
Change in the physical properties of hydrate-free sediments due to changes in effective stress and/or porosity after displacive hydrate formation - Physics-based correlations extracted from previous studies.

Property	Based on		Property^(after)/Property^(before)	Constitutive parameters (References)
Shear stiffness	Hertz	$G = \lambda\left(\frac{\sigma'}{kPa}\right)^{\beta}$	$\frac{G^a}{G^b} = \left(\frac{\sigma'^a}{\sigma'^b}\right)^{\beta}$	β = 0.25–0.45 (Cha et al., 2014)
Shear strength	Coulomb	$\tau = \sigma' \bullet tan\phi$	$\frac{\tau^a}{\tau^b} = \frac{\sigma'^a}{\sigma'^b}$	
Thermal conductivity	Geometric mean	$K_T = K_m^{1-n} \bullet K_f^n$	$\frac{K_T^a}{K_T^b} = \left(\frac{K_m}{K_f}\right)^{n_b - n_a}$	K_m/K_f = 3–5 for clay (Horai and Simmons, 1969; Waite et al., 2009)
Hydraulic conductivity	Kozeny-Carman	$K_H = \left(\frac{S_S}{\vartheta}\right)^{-2} e^{\chi}$	$\frac{K_H^a}{K_H^b} = \left(\frac{e^a}{e^b}\right)^{\chi}$	χ = 4–6 (Ren and Santamarina, 2018)
Electrical conductivity	Archie	$K_E = \varphi\, n^{\varsigma}\, K_f$	$\frac{K_E^a}{K_E^b} = \left(\frac{n^a}{n^b}\right)^{\varsigma}$	ς = 1.36 − 3.5(Lovell, 1985)

Note.
•Porosity $n = V_v/V_t$; void ratio $e = V_v/V_s$. Then: $n = e/(1 + e)$.
•Expressions assume that same constitutive parameters apply to the sediment before and after hydrate formation – Example: λ, β, tanϕ, χ, φ, ς, and specific surface S_s.
•The pore fluid electrical conductivity K_f increases due to ion exclusion during hydrate formation. However, we assume that ionic diffusion brings the pore fluid conductivity back to its original values in the long term, and K_f cancels in the final expression for the electrical conductivity ratio.

sediment compaction process and the hydrate volume fraction, as discussed above, and reflect physical correlations summarized in Table 1.

5.1. Conduction phenomena

Let's consider conduction phenomena so that flow q is a linear function of the gradient in the potential Ψ along the x_i direction,

$$q_i = K_i(x)A\frac{\partial \Psi}{\partial x_i} \tag{9}$$

where K is the conductivity and A is the cross sectional area (Note: the same analysis applies to thermal, hydraulic and electrical conduction).

Heat transfer studies in COMSOL modelled the medium with ~60,000 triangular 2D-elements (mesh size varies with lens configuration). The thermal conductivity is 2.6 $\mathrm{Wm^{-1}K^{-1}}$ for the water-saturated hydrate-free sediment, and 0.57 $\mathrm{Wm^{-1}K^{-1}}$ for the segregated hydrate mass (Note: the hydrate thermal conductivity K_T is similar to that of water, and four times smaller than the thermal conductivity of ice (Rosenbaum et al., 2007; Warzinski et al., 2008)).

Fig. 6 demonstrates the influence of a segregated hydrate lens on the temperature field: thermal conduction is significantly lower across the hydrate mass than in the surrounding sediment, therefore, temperature contour lines are closer to each other within the hydrate mass.

Fig. 7 compiles numerical simulation results for the effective thermal conductivity K_T as a function of lens orientation θ and hydrate volume fraction F_h. A single lens confers anisotropy to thermal conductivity, and the effective thermal conductivity K_T of the hydrate-bearing sediment tracks the analytical solution for anisotropy in layered media,

$$K_T = [\cos\theta \quad \sin\theta]\begin{bmatrix} K_0 & 0 \\ 0 & K_{90}\end{bmatrix}\begin{bmatrix}\cos\theta \\ \sin\theta\end{bmatrix} = K_0\cos^2\theta + K_{90}\sin^2\theta$$
$$= K_0 + (K_{90} - K_0)\sin^2\theta \tag{10}$$

where K_0 and K_{90} are the effective thermal conductivities of hydrate-bearing sediments when the lens is perpendicular $\theta = 0^{\circ}$ and parallel $\theta = 90^{\circ}$ to the thermal gradient. We simulated other segregated hydrate morphologies, such as two intersecting lenses that form a cross-shaped hydrate mass (refer to Figs. 2 and 3); in this case, the effective thermal conductivity of the hydrate-bearing sediment was not sensitive to orientation. These results correspond to elemental configurations that can be assembled to simulate hydrate morphologies in Figs. 2 and 3.

In general, the effect of sediment compaction around the hydrate lens can be equally or more important to the effective thermal conductivity of the medium than the orientation of the lens (refer to $K_T{}^b$ and $K_T{}^a$ in Fig. 7 and Table 2). The change in thermal conductivity $\Delta K_T = K_T{}^a – K_T{}^b$ is 0.2 $\mathrm{Wm^{-1}K^{-1}}$, while the effect of lens orientation is $\Delta K_T = K_{90} – K_0$ is 0.17 $\mathrm{Wm^{-1}K^{-1}}$ (thick lens - Fig. 7). This result highlights the effect of displacive hydrate formation and the ensuing

Table 2
Parameters used in analyses and numerical simulations. Values for sediments correspond to conditions after hydrate formation (Refer to Table 1).
Sources: (1) Huang and Fan, 2005, (2) Cortes et al., 2009, (3) Waite et al., 2009, (4) Helgerud et al., 2009, (5) Durham et al., 2003.

Property	Hydrate	Water-saturated sediment before hydrate formation	Water-saturated sediment after hydrate formation
Sediment Change (hydrate volume fraction F_h = 5% → σ'^a/σ'^b = 1.5)			
Void ratio	n/a	0.76	0.67
Stress [kPa]	n/a	300	450
Thermal			
Conductivity K_T [$\mathrm{W\,m^{-1}\,K^{-1}}$]	0.57 (1)	2.4 (2)	2.6 (2)
Heat Capacity C_p [$\mathrm{J\,kg^{-1}\,K^{-1}}$]	2031 (3)	1636[c]	1568[c]
Density ρ [$\mathrm{kg\,m^{-3}}$]	937	1937	1986
Mechanical			
Shear Modulus G [MPa]	3700 (4)	65	89
Elastic Modulus E [MPa]	9600 (4)	157 (drained)[a]	214 (drained)[a]
Bulk Modulus B [MPa]	8400 (4)	87 (drained)[a]	119 (drained)[a]
Poisson's Ratio ν [ ]	0.31 (4)	0.3 (large strain)	0.3 (large strain)
Yield, failure criterion	Elasto-plastic σ'_y = 25 MPa (5)	Cam Clay[b] $q = M\,p'$	

[a] From G assuming drained conditions and small-strain Poissons ratio of $\nu = 0.2$.
[b] Cam-clay parameters: compression index $C_c = 0.5$, void ratio at 1 kPa $e_{1kPa} = 2.0$, swelling index $C_s = 0.05$; failure stress ratio $M_f = 0.98$.
[c] Calculated by heat capacities of clay mineral $C_{pm} = 894\ \mathrm{J\,kg^{-1}\,K^{-1}}$ and water $C_{pw} = 4218\ \mathrm{J\,kg^{-1}\,K^{-1}}$ and their weight fractions $C_p = C_{pm}(1/(1 + w)) + C_{pw}(w/(1 + w))$, where w is the water content.

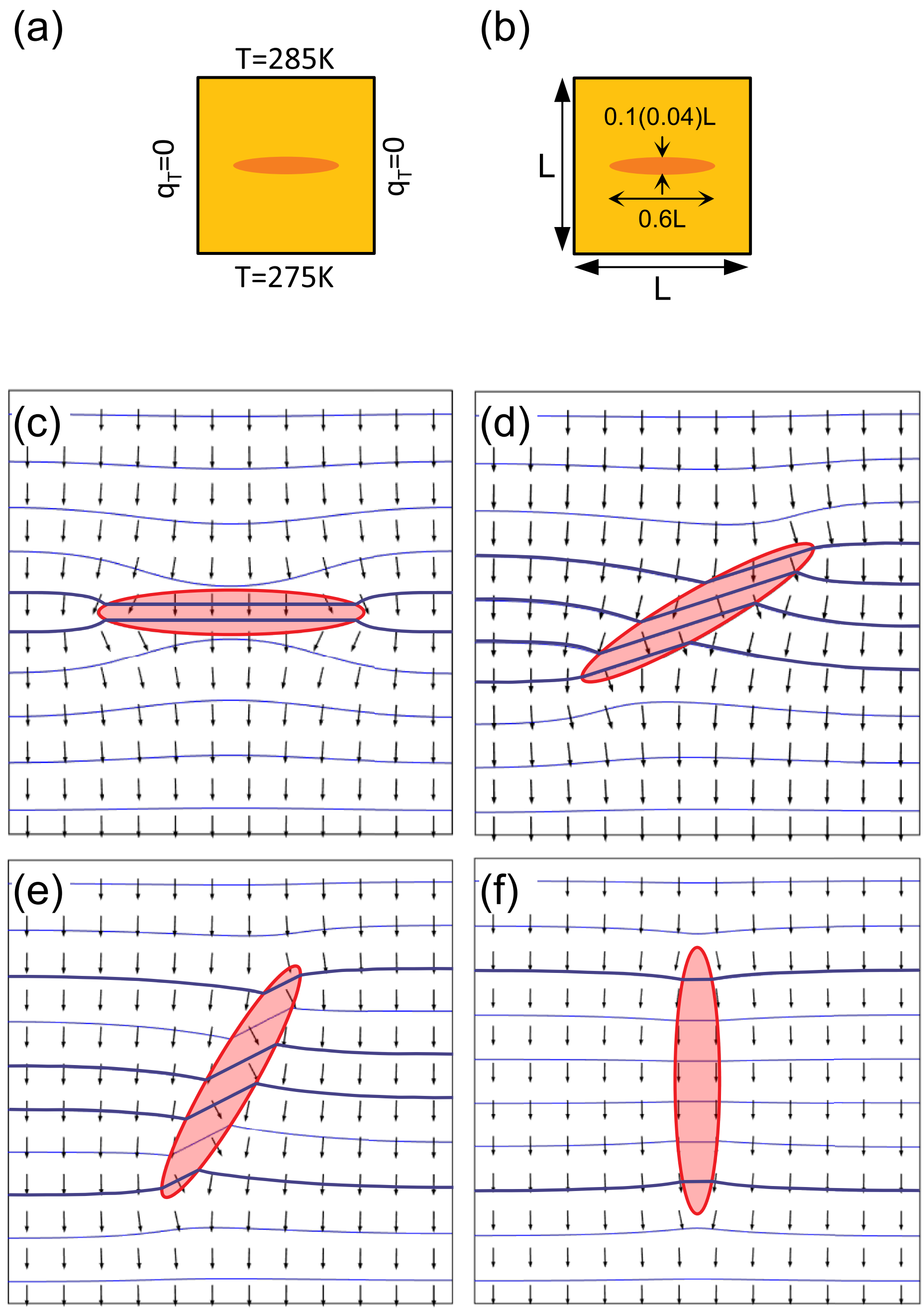

Fig. 6. Finite element simulation of heat conduction through fine-grained sediment with a segregated hydrate lens: (a) boundary conditions, (b) dimensions and (c–f) isotherm contours for hydrate lenses orientated at 0°, 30°, 60° and 90°. Arrows denote the direction of heat flow; transverse lines are equal-temperature contours; selected lines shown with thicker trace highlight the distortions of isotherm contours due to the presence of the hydrate lens.

changes in physical properties of the surrounding hydrate-free sediments (see Table 1).

The same numerical algorithm applies to other forms of conduction (Equation (9)). However, the hydraulic and electrical conductivities are much smaller for the hydrate mass than for the sediments; therefore, segregated hydrate lenses can cause pronounced reductions in hydraulic and DC electrical conductivities, as well as marked conductivity anisotropy in sediments.

5.2. Mechanical properties

Mechanical properties reflect internal equilibrium and deformation compatibility within the sediment mass in the presence of segregated hydrate lenses. We explore the two asymptotic conditions necessary for constitutive models and numerical simulations, i.e., small-strain stiffness and strength, using 2D numerical simulations (Abaqus, plane strain; 4-node bilinear CPE4; ~3300 elements in stiffness simulations and ~8000 in strength studies).

Small-strain Stiffness. The effective Young's modulus $E = \Delta\sigma_z/\Delta\varepsilon_z$ relates a change in axial stress $\Delta\sigma_z$ to the resultant axial strain $\Delta\varepsilon_z$. For the purposes of small-strain response, the elastic hydrate mass is assumed to be “bonded” to the elastic soil mass so that there is no interface slippage. The stiffness of each component corresponds to the value inferred from shear wave velocity (Table 2). Fig. 8 presents the influence of an elliptical hydrate lens on the drained Young's modulus of hydrate-bearing sediment, for two volume fractions and lenses at different orientations θ. The Young's modulus is highest when lenses are aligned with the loading z-direction, i.e., $\theta = 90°$, and increases with

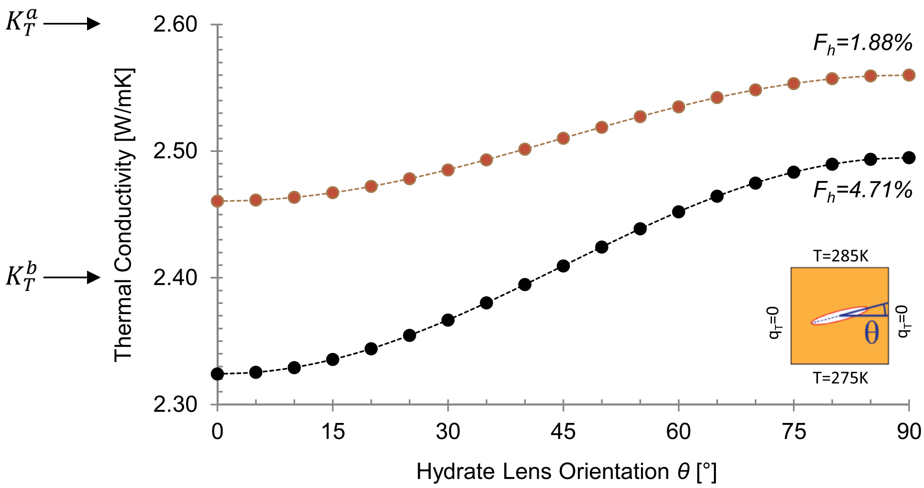

Fig. 7. Thermal conductivity in the vertical direction in a fine-grained sediment with a segregated hydrate lens as a function of lens orientation θ. Comparison between numerical simulation results (dots) and the analytical trend for anisotropic materials (lines - Equation (10)). Model parameters in Table 2 (The initial condition and all parameters correspond to a sediment subjected to 450 kPa).

hydrate saturation. Both simulations use the same sediment properties, therefore, the gap between the two trends is due to the hydrate mass only (differences in sediment stiffness associated with cryogenic suction would increase the separation between the two trends). The hydrate-sediment mechanical interaction is relevant at high lens inclinations only, and the stiffness anisotropy follows a $\sin^2\theta$ trend (Fig. 8 - For comparison, thermal conductivity is not affected by interfacial mechanics, and its anisotropy follows $\sin^6\theta$ trend - Equation (10), Fig. 7).

The bulk modulus $B = \Delta\sigma_o/\Delta\varepsilon_{vol}$ is the ratio between a change in isotropic stress $\Delta\sigma_o$ and the induced volumetric strain $\Delta\varepsilon_{vol}$. Deformation compatibility and stress equilibrium affect the internal stress field and the effective bulk stiffness of the hydrate-bearing sediment; consequently, the bulk modulus depends on the hydrate morphology and volume fraction. Numerical simulations confirm the effect of morphology for the same hydrate volume fraction F_h = 4.7% (3D, non-slip interface): a single elliptical lens (as in Fig. 6), and two intersecting flat hydrate layers that form a cross at the center of the specimen. Studies of hydrate morphology are conducted for the same type of interface to explore the independent contributions of morphology and interface. The numerically computed bulk moduli are B = 182 MPa for the elliptical lens, and B = 269 MPa for the cross-shaped lens (For reference: Hashin-Shtrikman bounds are B_{up} = 271 MPa and B_{low} = 130 MPa; the parallel and series configurations predict B_{par} = 509 MPa and B_{ser} = 125 MPa).

Strength. We investigate the drained strength of hydrate bearing sediments assuming an elasto-plastic hydrate behavior and "modified cam-clay" response for the surrounding sediment (cryogenically compacted to 450 kPa; parameters in Table 2 – Note: the failure conditions in Cam-Clay satisfy the frictional Mohr-Coulomb criterion, while volumetric and shear strains are physically linked through the yield surface). Simulations include two interface conditions between the hydrate mass and the surrounding sediment. The first interface is a non-slip condition and applies to rough and jagged lens morphology (Figs. 2 and 3); in this case, elements that form the hydrate lens share the same nodes as soil elements. The second interface is a "low friction" condition that is particularly relevant to smooth interfaces and dissociation studies; its simulation involves a thin Mohr-Coulomb layer with friction angle ϕ = 5°.

Images in Fig. 9 show the strain field superimposed on distorted specimens with an elliptical hydrate lens (Note: simulations run on a 2.5:1 specimen slenderness). Fig. 9 summarizes the effect of interfacial conditions and lens orientation on strength mobilization at two vertical strain levels ε_z = 5% and ε_z = 10%, before strain localization causes numerical instability. Results show:

- Non-slip interface: the presence of the hydrate mass has a minor effect on the mobilized specimen strength (both at ε_z = 5% and ε_z = 10%). The lens rotates clockwise during deviatoric loading and

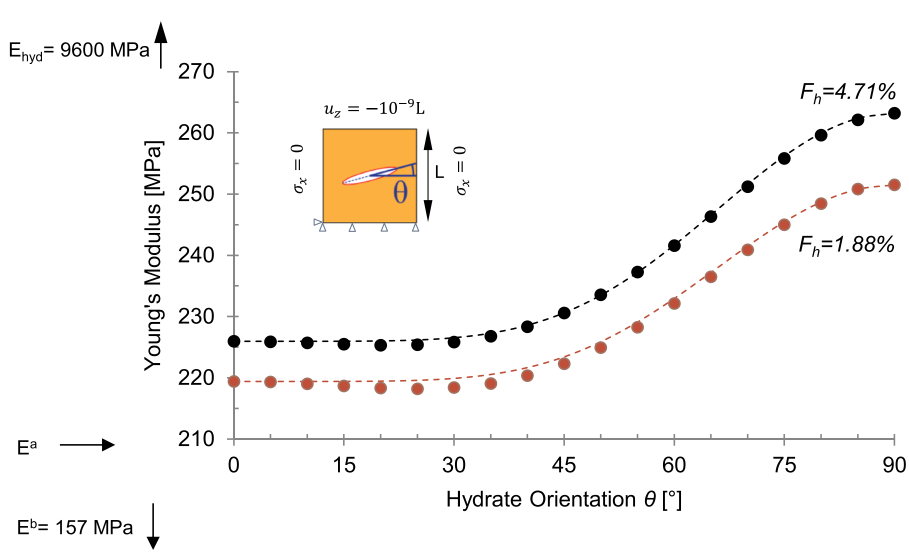

Fig. 8. Young's modulus of a fine-grained sediment with a segregated hydrate lens as a function of lens orientation θ for two hydrate saturations F_h. Dots show numerical simulation results. The lines show the trend predicted with $E = E_0 + (E_{90} - E_0)\sin^6\theta$. The initial condition and all parameters correspond to a sediment subjected to 450 kPa. Model parameters in Table 2.

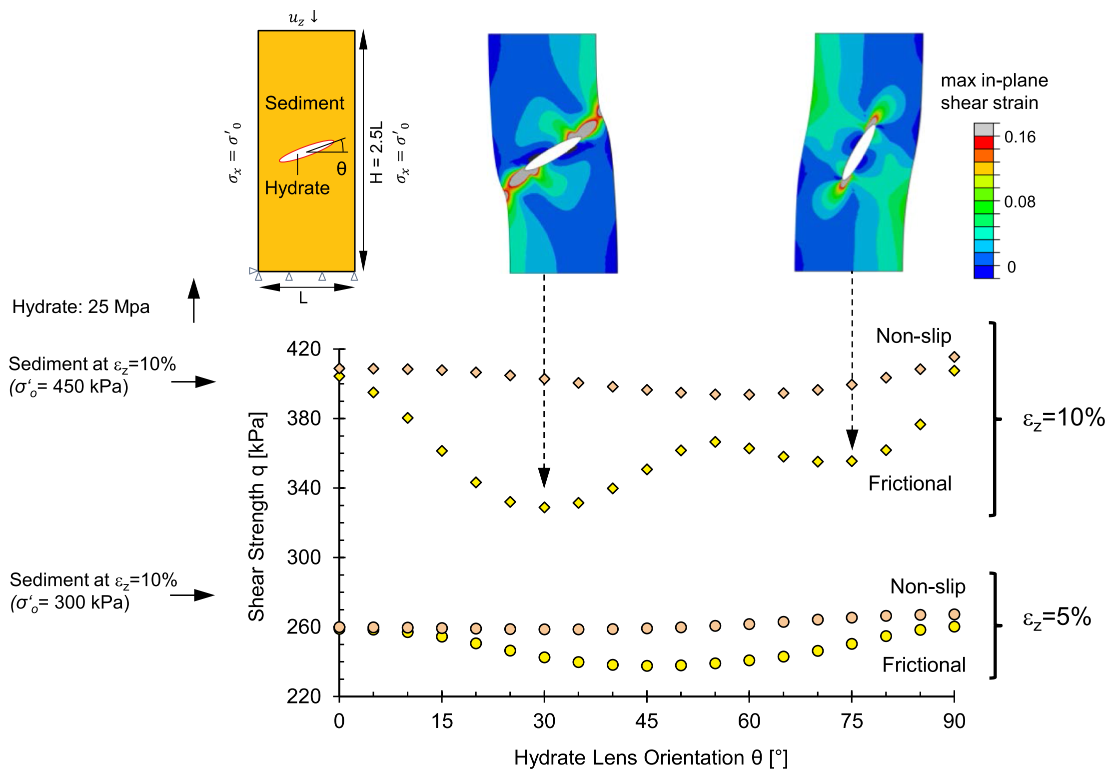

Fig. 9. Drained shear strength of a fine-grained sediment with an elliptical hydrate lens as a function of lens orientation θ for both low-friction and bonded interface conditions. Dots represent numerical simulation results reported at vertical strains $\varepsilon_z = 5\%$ and $\varepsilon_z = 10\%$. The upper images show the geometry and boundary conditions (left), and the numerically computed strain fields superimposed on two deformed specimens (right). The initial condition and all parameters correspond to a sediment subjected to 450 kPa, hydrate saturation $F_h = 4.71\%$. Model parameters in Table 2.

the upper part of the specimen deforms to the right. As rotation takes place, the vertical load shifts away from the centerline and causes a second moment effect. Second moment effects due to high deformation at $\varepsilon_z = 10\%$ cause a decrease in the "measured" strength for intermediate lens orientations.

- Low-friction interface: A lens with a low-friction interface weakens the specimen regardless of orientation. Large strains develop in the sediment near the lens tips and the specimen strength is severely diminished when the lens orientation favors slippage along the hydrate-sediment interface when the angle is $\approx 30°$. Two distinct deformed shapes evolve at $\varepsilon_z = 10\%$: the upper half slips along the lens and moves to the left of the specimen for $\theta \leq 45°$; however, the lens clockwise rotation prevails at $\theta \geq 60°$ and the specimen deforms to the right (Note: for a sediment friction $\phi = 25°$, failure takes place at an angle $45° + \phi/2 = 57.5°$). Large specimen deformations at $\varepsilon_z = 10\%$ cause second moment effects and lead to strength minima for lens orientations around $\theta \approx 30°$ and $\theta \approx 70°$.
- The effect of sediment strengthening due to cryogenic compaction is more pronounced on the specimen strength (shown on the left of Fig. 9) than the effect of the segregated hydrate mass, at least for these low hydrate saturations and for the assumed boundary conditions during hydrate formation.

More complex hydrate mass morphologies aggravate the need for numerical simulations to infer the physical properties of sediments with segregated hydrate lenses. Consider the case of two-intersecting hydrate lenses shown in Fig. 10:

- Bonded-interface: the steep lens experiences high stress as the soil wedge "hangs" from the stiffer hydrate mass (Fig. 10 – left).
- Low-friction interface: The upper sediment wedge slips along the steep lens, rests on the transverse lens and subjects it to high shear (Fig. 10 – right).

Once again, interface conditions and lens orientation affect the sediment-hydrate interaction. Also note pronounced differences in the sediment deformation in both cases.

6. Discussion

This section expands the scope of fine-grained sediments to fines-controlled sediments, assesses the applicability of effective media models and theoretical bounds, and suggests a reliable procedure for the estimation of the physical properties of fine-grained hydrate-bearing sediments.

6.1. Fines controlled?

There is evidence of segregated hydrate lenses in a wide range of sediments, besides homogeneous clays. In fact, fines can control both the mechanical and hydraulic properties of sediments even at relatively small mass fractions. For example, less than 10% of low-plasticity kaolinite is enough to control the hydraulic conductivity of sand, and by the time the kaolinite mass fraction reaches ~30%, the fines determine both mechanical and fluid flow properties (Park and Santamarina, 2017). These critical fines fractions are even lower for higher plasticity fines. Therefore, the fines fraction and the type of fines play a critical role on hydrate formation and ensuing properties.

Expeditions in the Krishna-Godavari Basin offshore India, the Ulleung Basin offshore South Korea, the Nankai Trough offshore Japan, and the Gulf of Mexico have frequently found significant fines contents in sediments labelled as "sands/silts" (Bahk et al., 2013; Flemings et al., 2018; Ito et al., 2015; Winters et al., 2014). Given the controlling role of fines, sediment characterization must emphasize the mass fraction of fines and their plasticity. The revised soil classification system RSCS properly captures the importance of fines on the sediment response (Park and Santamarina, 2017; Jang and Santamarina, 2016a).

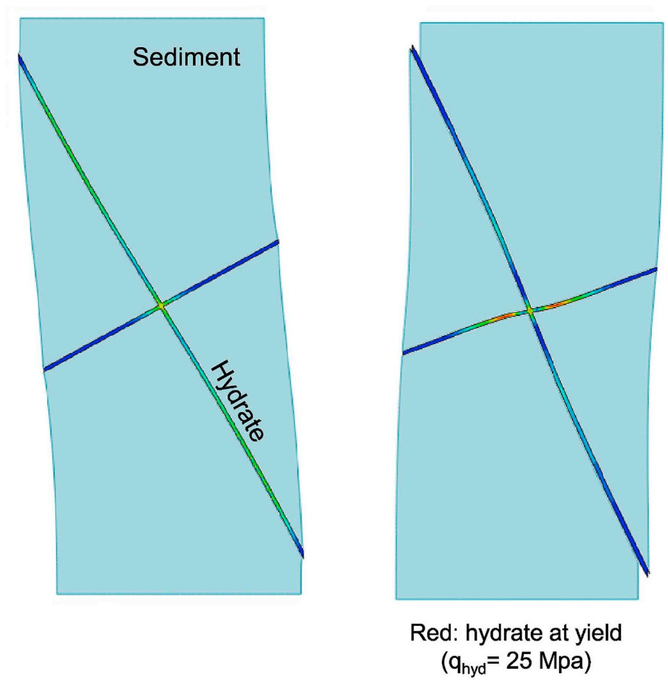

Fig. 10. Fine-grained sediments with a cross-shaped hydrate lens subjected to 10% vertical strain. (a) Non-slip interface. (b) Low-friction hydrate-sediment interface. The color scale ranges from gray to red with increasing intensity of the shear stress. Cross lenses deform together with the surrounding sediments and experience localized stress close to the lens intersection. Note: same boundary condition as in Fig. 9. The initial condition and all parameters correspond to a sediment subjected to 450 kPa, hydrate saturation $F_h = 4.71\%$. See Table 2 for model parameters. (For interpretation of the references to color in this figure legend, the reader is referred to the Web version of this article.)

6.2. *Effective media models – theoretical bounds*

Effective media models and theoretical bounds facilitate the estimation of the physical properties of hydrate-bearing sediments, and are valuable alternatives/complements to numerical simulations. Table 3 summarizes salient models and upper-lower bound estimates for the properties of segregated-hydrate bearing fine-grained sediments (details in Lei, 2017). Underlying assumptions focus on the distribution of phases: inclusions such as spheres, needles, disks and penny cracks (Berryman, 1980a, 1980b; Walpole, 1969; Walsh, 1965; Wu, 1966); homogeneous inclusion distribution in self-consistent models (Berryman, 1995; Ghosh et al., 2010). The Hashin-Shtrikman bounds are often preferred over the broader parallel and series bounds (Hashin and Shtrikman, 1962, 1963). However, the presence of segregated hydrate lenses often renders parameters that fall closer to the outer parallel and series bounds (for example, see thermal conductivity data in Cortes et al., 2009); in other words, the narrower Hashin-Shtrikman bounds do not always constrain the physical properties of sediments in the presence of segregated hydrate lenses.

6.3. *Suggested procedure to estimate the properties of sediments with segregated hydrate*

Analyses in previous sections show that displacive hydrate formation changes the physical properties of the surrounding hydrate-free sediment, and often confers the medium anisotropic behavior. The following steps provide guidelines for the estimation of physical properties (refer to previous sections for details):

- Assess whether the sediment is fines-controlled. If it is fines-controlled, assume various segregated hydrate morphologies and volume fractions.
- Consider boundary conditions during hydrate formation, estimate the stress and void ratio changes associated with hydrate formation,

Table 3
Summary of physical models and bounds for elastic parameters and conductivities – Compiled from previous studies.

Kuster and Toksoz (1) ♣	$(B_T - B_m)(B_m + 4G_m/3)/(B_T + 4G_m/3) = \sum F_i(B_i - B_m)P_i^m$ $(G_T - G_m)(G_m + \zeta_m)/(G_T + \zeta_m) = \sum F_i(G_i - G_m)Q_i^m$
Self-consistent [(2)] *For elastic parameters* ♣	$\sum F_i(B_i - B_T)P_i^m = 0$ $\sum F_i(G_i - G_T)Q_i^m = 0$
Self-consistent [(2)] *For conductivities* ♣	$\sum F_i(K_i - K_T)Z_i = 0$
Hashin Shtrikman Bounds *For elastic parameters* [(3)] ♠	$B_T^{\pm} = B_1 + F_2/[(B_2 - B_1)^{-1} + 3F_1(3B_1 + 4G_1)^{-1}]$ $G_T^{\pm} = G_1 + F_2/[(G_2 - G_1)^{-1} + 6F_1(B_1 + 2G_2)/[5G_1(3B_1 + 4G_1)]]$
Hashin Shtrikman Bounds *For conductivities* [(4)] ♠	$K_T^{\pm} = K_1 + F_2/[(K_2 - K_1)^{-1} + F_1/3K_2]$
Parallel and Series Bounds	Upper: $K_T = \sum F_i K_i$ Lower: $K_T^{-1} = \sum F_i K_i^{-1}$

	Spherical	Needle	Disk
Bulk Modulus P_i^m	$\frac{(B_m + 4G_m/3)}{(B_i + 4G_m/3)}$	$\frac{(B_m + G_m + G_i/3)}{(B_i + G_m + G_i/3)}$	$\frac{(B_m + 4G_i/3)}{(B_i + 4G_i/3)}$
Shear Modulus Q_i^m	$\frac{(G_m + \zeta_m)}{(G_i + \zeta_m)}$	$\frac{1}{5}\left(\frac{4G_m}{G_i + G_m} + 2\frac{G_m + \vartheta_m}{G_i + \vartheta_m} + \frac{B_i + 4G_m/3}{B_i + G_m + G_i/3}\right)$	$\frac{(G_m + \zeta_i)}{(G_i + \zeta_i)}$
Conductivities Z_i	$\frac{1}{(K_i + 2K_T)}$	$\frac{1}{9}\left(\frac{1}{K_T} + \frac{4}{(K_i + K_T)}\right)$	$\frac{1}{9}\left(\frac{1}{K_i} + \frac{2}{K_T}\right)$

Parameters $\vartheta = G\frac{3B + G}{3B + 7G}$ $\quad \zeta = \frac{G}{6}\frac{9B + 8G}{B + 2G}$

Note.

♣ Randomly orientated inclusion shapes: spheres, needles, disks and penny crack.

♠ Upper and lower bounds: switch components.

Volume fraction F, bulk modulus B, shear modulus G and conductivity K.

Subscripts: total medium T, constituent with max or min value m, and ith constituent.

Shape factors P, Q and Z for the Kuster-Toksoz and self-consistent models.

Sources: (1) Kuster and Toksöz, 1974; (2) Berryman, 1980a; (3) Hashin and Shtrikman, 1963; (4) Hashin and Shtrikman, 1962. General reference: Mavko et al., 2009.

and compute the modified properties for the hydrate-free sediment that surrounds the hydrate mass.
- Use numerical simulations or analytical models to compute the properties of the hydrate-bearing sediment. Consider hydrate configurations that are both parallel and normal to the imposed gradients or stresses. Vary hydrate-sediment interfacial conditions to represent field conditions of interest (e.g., rough and weak-frictional).
- Adopt an anisotropic variation with lens orientation θ that reflects the morphology of the hydrate mass.

7. Conclusions

The physical properties of hydrate-bearing sediments are critical for the analysis of mechanical stability and settlement, heat and fluid flow evaluations, and the design of gas production strategies. However, the assessment of physical properties is particularly challenging in fine-grained sediments due to (1) inherent difficulties in hydrate formation in the laboratory, and (2) specimen size requirements for a representative volume in fine-grained sediments with segregated gas hydrate. This study has circumvented these limitations by combining conceptual models and numerical simulations, leading to the conclusions below:

- Hydrate formation is grain-displacive when $\sigma' R < 2\pi\Gamma_{hw} \approx$ 0.2-to-0.3 N/m. Therefore, segregated hydrate is to be expected in fine-grained sediments (small R) and/or shallow formations (low σ'). Field evidence confirms this observation.
- Fines control the sediment mechanical and transport responses even at a relatively small fines fraction. Fines-controlled sediments are prone to segregated hydrate formation. In fact, sediments may exhibit hydrate lenses even when 80–90% of their mass is sand.
- Grain-displacive hydrate growth and cryogenic suction alter the physical properties of the "hydrate-free" sediment that surrounds the segregated hydrate mass. Stress and fluid flow boundary conditions determine the changes in effective stress and void ratio for a given hydrate volume fraction.
- The physical changes in the surrounding hydrate-free sediment can be more important on overall sediment properties than the presence of hydrate itself, as shown for the cases of strength and thermal conductivity. Thus, numerical simulations and effective media models need to consider both the hydrate morphology and the updated properties of the sediments around segregated hydrates.
- The effect of segregated hydrate on effective media properties reflects the hydrate morphology (shape, persistence, thickness, orientation), the physical properties of both the hydrate and sediment, and the interaction between the hydrate mass with the sediment. In the case of mechanical properties, this interaction implies compatibility of deformations and equilibrium (as highlighted by bulk modulus estimations); in the case of transport properties it implies continuity and conservation (heat, mass, and charge).
- Sediments with parallel hydrate lenses exhibit anisotropic conduction and mechanical properties, however anisotropy is less pronounced when lenses form intersecting cross-configurations.
- Laboratory formation and recovered cores show that the interface between the segregated hydrate and the surrounding sediment is rough and jagged. Yet, hydrate-sediment interaction evolves during dissociation and very low frictional resistance is anticipated at the hydrate-sediment interface.

Acknowledgements

Support for this research was provided by the U.S. Department of Energy, the Goizueta Foundation, and the KAUST endowment. Lingli Pan tested numerical simulations. Gabrielle E. Abelskamp edited the manuscript. All the data used in this article are included in the tables and figures.

Notation

A	Cross sectional area
B	Bulk modulus (Subscripts: low & up: Hashin-Shtrikman bounds; par & ser: parallel and series)
C_Δ	Hydrate-water pressure difference against the grain's cross-sectional area
C_Γ	Pull due to hydrate-water interfacial tension Γ_{hw} around the grain perimeter
C	Gas concentration (Superscripts: b = before and a = after hydrate formation)
C_c	Compression index of hydrate free sediments
C^H	Concentration of methane in hydrate
e	Void ratio (Superscripts b&a = before and after hydrate formation. Subscript: 0 = in situ)
E	Young's modulus
F_h	Hydrate volume fraction
G	Shear modulus of virgin sediments
H	Burial depth
k_o	Lateral earth pressure coefficient (Subscripts: o = at rest, p = at passive failure)
K	Conductivity
K_T	Thermal conductivity (Subscripts: hyd = hydrate, ice = ice, w = water. Superscripts: b = before and a = after hydrate formation)
K_0	Effective thermal conductivity of hydrate-bearing sediment (Subscript: 0 = when the lens is perpendicular and 90 = when the lens is parallel to the thermal gradient)
L	Hydrate lens length
n	Global porosity (Subscript 0 = initial)
N	Skeletal force
P_h	Pressure in the hydrate mass
q	Flow rate
R	Grain radius
R_{pore}	Pore throat radius
s	Spacing between adjacent lenses
S_h	Hydrate saturation
t_h	Lens thickness
u_w	Pressure in water
V	Volume (Subscripts: h = hydrate, t = total sediment volume, v = voids)
x_i	ith direction in the coordination
α	Ratio between pore radius and grain radius
ε	Strain (Subscript: z = axial in z direction, vol = volumetric)
ϕ	Sediment friction angle
Γ_{hw}	Hydrate-water interfacial tension
ν	Poisson's ratio of virgin sediments
θ	Lens orientation
σ'	Effective stress (Superscripts: b = before and a = after hydrate formation. Subscripts: 0 = isotropic, z = vertical, hor = horizontal, nor = normal to lens, 1 = major principal)
Ψ	Potential

References

Anderson, R., Llamedo, M., Tohidi, B., Burgass, R.W., 2003. Experimental measurement of methane and carbon dioxide clathrate hydrate equilibria in mesoporous silica. J. Phys. Chem. B 107 (15), 3507–3514. https://doi.org/10.1021/jp0263370.

Archer, D., 2007. Methane hydrate stability and anthropogenic climate change. Biogeosciences 4 (4), 521–544. https://doi.org/10.5194/bg-4-521-2007.

Bahk, J.J., Kim, D.H., Chun, J.H., Son, B.K., Kim, J.H., Ryu, B.J., et al., 2013. Gas hydrate occurrences and their relation to host sediment properties: results from second Ulleung basin gas hydrate drilling expedition, East Sea. Mar. Pet. Geol. 47, 21–29. https://doi.org/10.1016/j.marpetgeo.2013.05.006.

Berryman, J.G., 1980a. Long-wavelength propagation in composite elastic media I. Spherical inclusions. J. Acoust. Soc. Am. 68 (6), 1809–1819. https://doi.org/10.1121/1.385171.

Berryman, J.G., 1980b. Long-wavelength propagation in composite elastic media II. Ellipsoidal inclusions. J. Acoust. Soc. Am. 68 (6), 1820–1831. https://doi.org/10.

1121/1.385172.
Berryman, J.G., 1995. Mixture theories for rock properties. In: Ahrens, T.J. (Ed.), Rock Physics & Phase Relations: A Handbook of Physical Constants. American Geophysical Union, Washington, DC, pp. 205–228. https://doi.org/10.1029/RF003p0205.
Bohrmann, G., Suess, E., Greinert, J., Teichert, B., Naehr, T., 2002. Gas hydrate carbonates from Hydrate Ridge, cascadia convergent margin: indicators of near-seafloor clathrate deposits. In: Proceedings of the 4th International Conference on Gas Hydrates (ICGH 2002), Yokohama, Japan.
Boswell, R., 2009. Is gas hydrate energy within reach? Science 325 (5943), 957–958. https://doi.org/10.1126/science.1175074.
Boswell, R., Collett, T.S., 2011. Current perspectives on gas hydrate resources. Energy Environ. Sci. 4 (4), 1206–1215. https://doi.org/10.1039/C0EE00203H.
Boswell, R., Kleinberg, R., Collett, T., Frye, M., 2007. Exploration priorities for marine gas hydrate resources. Fire in the Ice 7 (2), 11–13. https://www.netl.doe.gov/sites/default/files/publication/HMNewsSpringSummer07.pdf.
Cha, M., Santamarina, J.C., Kim, H.-S., Cho, G.-C., 2014. Small-strain stiffness, shear-wave velocity, and soil compressibility. J. Geotech. Geoenviron. Eng. 140 (10), 06014011. https://doi.org/10.1061/(ASCE)GT.1943-5606.0001157.
Clennell, M.B., Hovland, M., Booth, J.S., Henry, P., Winters, W.J., 1999. Formation of natural gas hydrates in marine sediments: 1. Conceptual model of gas hydrate growth conditioned by host sediment properties. J. Geophys. Res.: Solid Earth 104 (B10), 22985–23003. https://doi.org/10.1029/1999JB900175.
Collett, T.S., 2002. Energy resource potential of natural gas hydrates. AAPG (Am. Assoc. Pet. Geol.) Bull. 86 (11), 1971–1992. https://doi.org/10.1306/61EEDDD2-173E-11D7-8645000102C1865D.
Collett, T.S., Riedel, M., Cochran, J.R., Boswell, R., Kumar, P., Sathe, A.V., 2008. Indian continental margin gas hydrate prospects: results of the Indian national gas hydrate program (NGHP) expedition 01. In: Proceedings of the 6th International Conference on Gas Hydrates (ICGH 2008), Vancouver, British Columbia, Canada.
Cook, A.E., Goldberg, D., Kleinberg, R.L., 2008. Fracture-controlled gas hydrate systems in the northern Gulf of Mexico. Mar. Pet. Geol. 25 (9), 932–941. https://doi.org/10.1016/j.marpetgeo.2008.01.013.
Cortes, D.D., Martin, A.I., Yun, T.S., Francisca, F.M., Santamarina, J.C., Ruppel, C., 2009. Thermal conductivity of hydrate-bearing sediments. J. Geophys. Res.: Solid Earth 114 (B11), B11103. https://doi.org/10.1029/2008JB006235.
Dai, S., Santamarina, J.C., 2014. Sampling disturbance in hydrate-bearing sediment pressure cores: NGHP-01 expedition, Krishna–Godavari Basin example. Mar. Pet. Geol. 58, 178–186. https://doi.org/10.1016/j.marpetgeo.2014.07.013.
Dai, S., Santamarina, J.C., Waite, W.F., Kneafsey, T.J., 2012. Hydrate morphology: physical properties of sands with patchy hydrate saturation. J. Geophys. Res.: Solid Earth 117 (B11), B11205. https://doi.org/10.1029/2012JB009667.
Duan, Z., Mao, S., 2006. A thermodynamic model for calculating methane solubility, density and gas phase composition of methane-bearing aqueous fluids from 273 to 523K and from 1 to 2000bar. Geochem. Cosmochim. Acta 70 (13), 3369–3386. https://doi.org/10.1016/j.gca.2006.03.018.
Duan, Z., Sun, R., 2003. An improved model calculating CO_2 solubility in pure water and aqueous NaCl solutions from 273 to 533 K and from 0 to 2000 bar. Chem. Geol. 193 (3), 257–271. https://doi.org/10.1016/S0009-2541(02)00263-2.
Durham, W.B., Kirby, S.H., Stern, L.A., Zhang, W., 2003. The strength and rheology of methane clathrate hydrate. J. Geophys. Res.: Solid Earth 108 (B4), 2182. https://doi.org/10.1029/2002JB001872.
Flemings, P.B., Phillips, S.C., Collett, T., Cook, A., Boswell, R., the UT-GOM2-1 Expedition Scientists, 2018. UT-GOM2-1 hydrate pressure coring expedition hole GC 955 H002. In: Flemings, P.B. (Ed.), UT-GOM2-1 Hydrate Pressure Coring Expedition Report (Chap. 3). University of Texas Institute for Geophysics, Austin, TX. http://www-udc.ig.utexas.edu/gom2/Chapter%203%20-%20H002.pdf.
Gdoutos, E.E., 2006. Fracture Mechanics: an Introduction, second ed. Springer, Dordrecht, The Netherlands. https://doi.org/10.1007/1-4020-3153-X.
Ghosh, R., Sain, K., Ojha, M., 2010. Effective medium modeling of gas hydrate-filled fractures using the sonic log in the Krishna-Godavari basin, offshore eastern India. J. Geophys. Res.: Solid Earth 115 (B6), B06101. https://doi.org/10.1029/2009JB006711.
Grozic, J.L.H., 2010. Interplay between gas hydrates and submarine slope failure. In: Mosher, D.C. (Ed.), Submarine Mass Movements and Their Consequences (Chap. 2). Springer Science & Business Media, Dordrecht, The Netherlands, pp. 11–30. https://doi.org/10.1007/978-90-481-3071-9_2.
Hashin, Z., Shtrikman, S., 1962. A variational approach to the theory of the effective magnetic permeability of multiphase materials. J. Appl. Phys. 33 (10), 3125–3131. https://doi.org/10.1063/1.1728579.
Hashin, Z., Shtrikman, S., 1963. A variational approach to the theory of the elastic behaviour of multiphase materials. J. Mech. Phys. Solids 11 (2), 127–140. https://doi.org/10.1016/0022-5096(63)90060-7.
Helgerud, M.B., Waite, W.F., Kirby, S.H., Nur, A., 2009. Elastic wave speeds and moduli in polycrystalline ice Ih, sI methane hydrate, and sII methane-ethane hydrate. J. Geophys. Res.: Solid Earth 114 (B2), B02212. https://doi.org/10.1029/2008JB006132.
Henry, P., Thomas, M., Clennell, M.B., 1999. Formation of natural gas hydrates in marine sediments: 2. Thermodynamic calculations of stability conditions in porous sediments. J. Geophys. Res.: Solid Earth 104 (B10), 23005–23022. https://doi.org/10.1029/1999JB900167.
Horai, K.-i., Simmons, G., 1969. Thermal conductivity of rock-forming minerals. Earth Planet. Sci. Lett. 6 (5), 359–368. https://doi.org/10.1016/0012-821X(69)90186-1.
Hornbach, M.J., Lavier, L.L., Ruppel, C.D., 2007. Triggering mechanism and tsunamogenic potential of the Cape Fear Slide complex, U.S. Atlantic margin. Geochem. Geophys. Geosyst. 8 (12), Q12008. https://doi.org/10.1029/2007GC001722.
Huang, D., Fan, S., 2005. Measuring and modeling thermal conductivity of gas hydrate-bearing sand. J. Geophys. Res.: Solid Earth 110 (B1), B01311. https://doi.org/10.1029/2004JB003314.
Hvorslev, M.J., 1949. Subsurface Exploration and Sampling of Soils for Civil Engineering Purposes. Soil Mechanics and Foundations Division, American Society of Civil Engineers, Vicksburg, Mississippi.
Ito, T., Komatsu, Y., Fujii, T., Suzuki, K., Egawa, K., Nakatsuka, Y., et al., 2015. Lithological features of hydrate-bearing sediments and their relationship with gas hydrate saturation in the eastern Nankai Trough, Japan. Mar. Pet. Geol. 66, 368–378. https://doi.org/10.1016/j.marpetgeo.2015.02.022.
Jang, J., Santamarina, J.C., 2016a. Fines classification based on sensitivity to pore-fluid chemistry. J. Geotech. Geoenviron. Eng. 142 (4), 06015018. https://doi.org/10.1061/(ASCE)GT.1943-5606.0001420.
Jang, J., Santamarina, J.C., 2016b. Hydrate bearing clayey sediments: formation and gas production concepts. Mar. Pet. Geol. 77, 235–246. https://doi.org/10.1016/j.marpetgeo.2016.06.013.
Kuster, G.T., Toksöz, M.N., 1974. Velocity and attenuation of seismic waves in two-phase media: Part I. Theoretical formulations. Geophysics 39 (5), 587–606. https://doi.org/10.1190/1.1440450.
Kvalstad, T.J., Andresen, L., Forsberg, C.F., Berg, K., Bryn, P., Wangen, M., 2005. The Storegga slide: evaluation of triggering sources and slide mechanics. Mar. Pet. Geol. 22 (1), 245–256. https://doi.org/10.1016/j.marpetgeo.2004.10.019.
Kwon, T.-H., Cho, G.-C., Santamarina, J.C., 2008. Gas hydrate dissociation in sediments: pressure-temperature evolution. Geochem. Geophys. Geosyst. 9 (3), Q03019. https://doi.org/10.1029/2007GC001920.
Lee, C., Yun, T.S., Lee, J.-S., Bahk, J.J., Santamarina, J.C., 2011. Geotechnical characterization of marine sediments in the Ulleung basin, East Sea. Eng. Geol. 117 (1), 151–158. https://doi.org/10.1016/j.enggeo.2010.10.014.
Lee, J.Y., Jung, J.W., Lee, M.H., Bahk, J.J., Choi, J., Ryu, B.J., Schultheiss, P., 2013. Pressure core based study of gas hydrates in the Ulleung Basin and implication for geomechanical controls on gas hydrate occurrence. Mar. Pet. Geol. 47, 85–98. https://doi.org/10.1016/j.marpetgeo.2013.05.021.
Lei, L., 2017. *Gas Hydrate in Fine-Grained Sediments—Laboratory Studies and Coupled Processes Analyses.* (PhD). Georgia Institute of Technology, Atlanta Retrieved from. http://hdl.handle.net/1853/58215.
Lei, L., Santamarina, J.C., 2018. Laboratory strategies for hydrate formation in fine-grained sediments. J. Geophys. Res.: Solid Earth 123 (4), 2583–2596. https://doi.org/10.1002/2017JB014624.
Lei, L., Seol, Y., Choi, J.-H., Kneafsey, T.J., 2019. Pore habit of methane hydrate and its evolution in sediment matrix – laboratory visualization with phase-contrast micro-CT. Mar. Pet. Geol. 104, 451–467. https://doi.org/10.1016/j.marpetgeo.2019.04.004.
Lovell, M.A., 1985. Thermal conductivity and permeability assessment by electrical resistivity measurements in marine sediments. Mar. Geotechnol. 6 (2), 205–240. https://doi.org/10.1080/10641198509388187.
Lu, W., Chou, I.M., Burruss, R.C., 2008. Determination of methane concentrations in water in equilibrium with sI methane hydrate in the absence of a vapor phase by in situ Raman spectroscopy. Geochem. Cosmochim. Acta 72 (2), 412–422. https://doi.org/10.1016/j.gca.2007.11.006.
Makogon, Y.F., 1997. Hydrates of Hydrocarbons. Pennwell Books, PennWell Publishing Company, Tulsa, Oklahoma.
Mavko, G., Mukerji, T., Dvorkin, J., 2009. The Rock Physics Handbook: Tools for Seismic Analysis of Porous Media, second ed. Cambridge University Press, Cambridge. https://doi.org/10.1017/CBO9780511626753.
Mayne, P.W., Kulhawy, F.H., 1982. K_o-OCR relationships in soil. J. Geotech. Eng. Div. 108 (GT6), 851–869.
Moridis, G., Collett, T.S., Pooladi-Darvish, M., Hancock, S.H., Santamarina, C., Boswell, R., et al., 2011. Challenges, uncertainties, and issues facing gas production from gas-hydrate deposits. SPE Reserv. Eval. Eng. 14 (01), 76–112. https://doi.org/10.2118/131792-PA.
Park, J., Santamarina, J.C., 2017. Revised soil classification system for coarse-fine mixtures. J. Geotech. Geoenviron. Eng. 143 (8), 04017039. https://doi.org/10.1061/(ASCE)GT.1943-5606.0001705.
Park, K.-P., Bahk, J.-J., Kwon, Y., Kim, G.Y., Riedel, M., Holland, M., et al., 2008. Korean national program expedition confirms rich gas hydrate deposit in the Ulleung Basin, East Sea. Fire in the Ice 8 (2), 6–9. https://www.netl.doe.gov/sites/default/files/publication/HMNewsSpring08.pdf.
Rees, E.V.L., Priest, J.A., Clayton, C.R.I., 2011. The structure of methane gas hydrate bearing sediments from the Krishna–Godavari Basin as seen from Micro-CT scanning. Mar. Pet. Geol. 28 (7), 1283–1293. https://doi.org/10.1016/j.marpetgeo.2011.03.015.
Ren, X.W., Santamarina, J.C., 2018. The hydraulic conductivity of sediments: a pore size perspective. Eng. Geol. 233, 48–54. https://doi.org/10.1016/j.enggeo.2017.11.022.
Rosenbaum, E.J., English, N.J., Johnson, J.K., Shaw, D.W., Warzinski, R.P., 2007. Thermal conductivity of methane hydrate from experiment and molecular simulation. J. Phys. Chem. B 111 (46), 13194–13205. https://doi.org/10.1021/jp074419o.
Ruppel, C., Pohlman, J.W., 2008. Climate change and the global carbon cycle: perspectives and opportunities. Fire in the Ice 8 (1), 5–8. https://www.netl.doe.gov/sites/default/files/publication/HMNewsWinter08.pdf.
Santamarina, J.C., 2001. Soil behavior at the microscale: Particle forces. In: Symposium on Soil Behavior and Soft Ground Construction Honoring Charles C. "Chuck" Ladd, Cambridge, Massachusetts, United States, . https://doi.org/10.1061/40659(2003)2.
Santamarina, J.C., Klein, K.A., Fam, M.A., 2001. Soils and Waves: Particulate Materials Behavior, Characterization and Process Monitoring. John Wiley and Sons Ltd, Hoboken, United States.
Shin, H., Santamarina, J.C., 2009. Mineral dissolution and the evolution of k_0. J. Geotech. Geoenviron. Eng. 135 (8), 1141–1147. https://doi.org/10.1061/(ASCE)GT.1943-

5606.0000053.
Shin, H., Santamarina, J.C., 2011. Open-mode discontinuities in soils. Géotech. Lett. 1 (4), 95–99. https://doi.org/10.1680/geolett.11.00014.
Shoji, H., Minami, H., Hachikubo, A., Sakagami, H., Hyakutake, K., Soloviev, V., et al., 2005. Hydrate-bearing structures in the sea of Okhotsk. Eos, Trans. Am. Geophys. Union 86 (2), 13–18. https://doi.org/10.1029/2005EO020001.
Sloan, E.D., Koh, C.A., 2007. In: Heinemann, H. (Ed.), Clathrate Hydrates of Natural Gases, third ed. CRC Press, Boca Raton, FL. https://www.crcpress.com/Clathrate-Hydrates-of-Natural-Gases-Third-Edition/Sloan-Jr-Koh/p/book/9780849390784.
Spangenberg, E., Kulenkampff, J., Naumann, R., Erzinger, J., 2005. Pore space hydrate formation in a glass bead sample from methane dissolved in water. Geophys. Res. Lett. 32 (24), L24301. https://doi.org/10.1029/2005GL024107.
Sun, Z., Santamarina, J.C., 2019. Grain-displacive gas migration in fine-grained sediments. J. Geophys. Res.: Solid Earth 124 (3), 2274–2285. https://doi.org/10.1029/2018JB016394.
Tan, B., Germaine, J.T., Flemings, P.B., 2006. Data report: consolidation and strength characteristics of sediments from ODP Site 1244, Hydrate Ridge, Cascadia continental margin. In: Proceedings of the Ocean Drilling Program, Scientific Results, . http://www-odp.tamu.edu/publications/204_SR/VOLUME/CHAPTERS/102.PDF.
Tréhu, A.M., Long, P.E., Torres, M.E., Bohrmann, G., Rack, F.R., Collett, T.S., et al., 2004. Three-dimensional distribution of gas hydrate beneath southern Hydrate Ridge: constraints from ODP Leg 204. Earth Planet. Sci. Lett. 222 (3), 845–862. https://doi.org/10.1016/j.epsl.2004.03.035.
Uchida, T., Ebinuma, T., Ishizaki, T., 1999. Dissociation condition measurements of methane hydrate in confined small pores of porous glass. J. Phys. Chem. B 103 (18), 3659–3662. https://doi.org/10.1021/jp984559l.
Viggiani, G., Andò, E., Takano, D., Santamarina, J.C., 2015. Laboratory X-ray tomography: a valuable experimental tool for revealing processes in soils. Geotech. Test J. 38 (1), 61–71. https://doi.org/10.1520/GTJ20140060.
Waite, W.F., Santamarina, J.C., Cortes, D.D., Dugan, B., Espinoza, D.N., Germaine, J., et al., 2009. Physical properties of hydrate-bearing sediments. Rev. Geophys. 47 (4), RG4003. https://doi.org/10.1029/2008RG000279.
Waite, W.F., Spangenberg, E., 2013. Gas hydrate formation rates from dissolved-phase methane in porous laboratory specimens. Geophys. Res. Lett. 40 (16), 4310–4315. https://doi.org/10.1002/grl.50809.
Walpole, L.J., 1969. On the overall elastic moduli of composite materials. J. Mech. Phys. Solids 17 (4), 235–251. https://doi.org/10.1016/0022-5096(69)90014-3.
Walsh, J.B., 1965. The effect of cracks on the compressibility of rock. J. Geophys. Res. 70 (2), 381–389. 1896-1977. https://doi.org/10.1029/JZ070i002p00381.
Warzinski, R.P., Gamwo, I.K., Rosenbaum, E.J., Myshakin, E.M., Jiang, H., Jordan, K.D., et al., 2008. Thermal properties of methane hydrate by experiment and modeling and impacts upon technology. In: Proceedings of the 6th International Conference on Gas Hydrates (ICGH 2008), Vancouver, British Columbia, Canada.
Winters, W.J., Wilcox-Cline, R.W., Long, P., Dewri, S.K., Kumar, P., Stern, L., Kerr, L., 2014. Comparison of the physical and geotechnical properties of gas-hydrate-bearing sediments from offshore India and other gas-hydrate-reservoir systems. Mar. Pet. Geol. 58, 139–167. https://doi.org/10.1016/j.marpetgeo.2014.07.024.
Wu, T.T., 1966. The effect of inclusion shape on the elastic moduli of a two-phase material. Int. J. Solids Struct. 2 (1), 1–8. https://doi.org/10.1016/0020-7683(66)90002-3.
Yamamoton, K., Inada, N., Kubo, S., Fujii, T., Suzuki, K., Konno, Y., Shipboard Scientists for the Methane Hydrate Offshore Production Test, 2012. Pressure core sampling in the eastern Nankai Trough. Fire in the Ice 12 (2), 1–6. https://www.netl.doe.gov/sites/default/files/publication/MHNews_2012_Oct.pdf.
Yun, T.S., Lee, C., Lee, J.-S., Bahk, J.J., Santamarina, J.C., 2011. A pressure core based characterization of hydrate-bearing sediments in the Ulleung Basin, Sea of Japan (East Sea). J. Geophys. Res.: Solid Earth 116 (B2), B02204. https://doi.org/10.1029/2010JB007468.
Zhang, G., Yang, S., Zhang, M., Liang, J., Lu, J., Holland, M., et al., 2014. GMGS2 expedition investigates rich and complex gas hydrate environment in the South China Sea. Fire in the Ice 14 (1), 1–5. https://www.netl.doe.gov/sites/default/files/publication/MHNews_2014_February.pdf.